# Catalysis Science & **Technology**



**View Article Online PAPER** 



Cite this: Catal. Sci. Technol., 2018, 8,6228

# Catalytic oxidation of propane over palladium alloyed with gold: an assessment of the chemical and intermediate species†

Haval Kareem, a Shiyao Shan, a Zhi-Peng Wu, a Leslie Velasco, a Kelli Moseman, a Casey P. O'Brien, Dat T. Tran, Ivan C. Lee, Yazan Maswadeh, Lefu Yang, Derrick Mott, <sup>e</sup> Jin Luo, <sup>a</sup> Valeri Petkov <sup>b</sup> and Chuan-Jian Zhong <sup>a</sup>

Understanding the catalytic oxidation of propane is important for developing catalysts not only for catalytic oxidation of hydrocarbons in emission systems but also for selective oxidation in the chemical processing industry. For palladium-based catalysts, little is known about the identification of the chemical or intermediate species involved in propane oxidation. We describe herein findings of an investigation of the catalytic oxidation of propane over supported palladium nanoalloys with different compositions of gold (Pd<sub>n</sub>Au<sub>100-n</sub>), focusing on probing the chemical or intermediate species on the catalysts in correlation with the bimetallic composition and the alloying phase structure. In addition to an enhanced catalytic activity, a strong dependence of the catalytic activity on the bimetallic composition was revealed, displaying an activity maximum at a Pd: Au ratio of 50:50 in terms of reaction temperature. This dependence is also reflected by its dependence on the thermochemical treatment conditions. While the activity for nanoalloys with  $n\sim$ 50 showed little change after the thermochemical treatment under oxygen, the activities for nanoalloys with n < 50 and n > 50 showed opposite trends. Importantly, this catalytic synergy is linked to the subtle differences of chemical and intermediate species which have been identified for the catalysts with different bimetallic compositions by in situ measurements using diffuse reflectance infrared Fourier transform spectroscopy (DRIFTS). For the catalytic oxidation of propane over the highly-active catalyst with a Pd: Au ratio of 50:50, the major species identified include acetate and bicarbonate, showing subtle differences in comparison with the identification of bicarbonate and formate for the catalyst with <50% Au (with a lower activity) and the absence of apparent species for the catalyst with >50% Au (activity is largely absent). The alloying of 50% Au in Pd is believed to increase the oxophilicity of Pd, which facilitates the first carbon-carbon bond cleavage and oxygenation of propane. The implications of the findings on the catalytic synergy of Pd alloyed with Au and the design of active Pd alloy catalysts are also discussed.

Received 15th August 2018, Accepted 25th October 2018

DOI: 10.1039/c8cv01704b

rsc.li/catalysis

### 1. Introduction

Emissions from vehicles and power stations using liquefied petroleum gas (LPG) are the main source of harmful volatile organic compounds (VOC)s.1,2 With increasingly rigorous emission standards, effective catalytic oxidation of VOCs is increasingly important.<sup>3,4</sup> In comparison with Pt, Pd is known for its activity for many reactions including propane oxidation due to its resistance to poisoning by traces of CO5 and its tolerance to moisture.6 However, deactivation still constitutes a major challenge. In a recent study<sup>7</sup> of the catalytic activity of Pd and Rh for CO and propane oxidation, the activity is shown to decrease at high temperature due to agglomeration of the nanoparticles as a result of metal oxidation. In another study,8 the low activity of propane oxidation over pure Pd/ Al<sub>2</sub>O<sub>3</sub> was ascribed to sintering and reducibility of the active site  $PdO_x$  and generation of metallic  $Pd^0$ . Bimetallic catalysts are considered a promising alternative in terms of stability and high activity in comparison with monometallic Pd.9 In a study by Lang et al.,10 nanoporous AuPd showed higher catalytic activity and improved electrochemical stability toward

<sup>&</sup>lt;sup>a</sup> Department of Chemistry, State University of New York at Binghamton, Binghamton, New York 13902, USA. E-mail: cjzhong@binghamton.edu

<sup>&</sup>lt;sup>b</sup> Department of Physics, Central Michigan University, Mt. Pleasant, Michigan

<sup>&</sup>lt;sup>c</sup> U.S. Army Research Laboratory, Sensors and Electron Devices Directorate, Adelphi, MD 20783, USA

<sup>&</sup>lt;sup>d</sup> College of Chemistry and Chemical Engineering, Xiamen University, Xiamen

<sup>&</sup>lt;sup>e</sup> School of Materials Science, Japan Advanced Institute of Science and Technology, Nomi, Ishikawa 923-1292, Japan

<sup>†</sup> Electronic supplementary information (ESI) available: Additional HAADF-STEM image, catalytic activity data (Fig. S1-S4), DRIFTS data (Fig. S5 and S6; Tables S1 and S2), and DFT calculation data (Tables S3 and S4). See DOI: 10.1039/ c8cy01704b

methanol oxidation. Similarly, Co<sub>3</sub>O<sub>4</sub>-supported AuPd showed higher catalytic activity and better stability than supported Au and Pd for toluene oxidation due to a strong interaction between AuPd and the support.11 Promotion of the catalytic activity of noble metals such as Pt and Pd with low-cost transition metals such as Ni, Cu, Co, etc. was observed. However, long-term durability is an issue due to the degradation of the catalyst. 12 On the other hand, supports have been shown to exhibit significant effects on the catalytic activity of nanoparticles, including providing oxygen during propane oxidation (e.g., TiO<sub>2</sub> or CeO<sub>2</sub>)<sup>13</sup> or assisting the generation of active species.14 Also, the acid/base strength of the support is shown to influence the catalytic performance in terms of dispersion and the oxidation state of the supported Pd or Pt. In a study by Yoshida et al., 15 the effects of the support (MgO, Al<sub>2</sub>O<sub>3</sub>, SiO<sub>2</sub>-Al<sub>2</sub>O<sub>3</sub>) and additives on the catalytic activity of propane oxidation were investigated, showing that the catalyst performance is enhanced with a more acidic support and with higher electronegativity of the additives. To increase the activity and stability, the alloying of Pd with Au has been considered an important approach since Au has a higher oxidation potential than Pd. While PdAu has been studied for many catalytic reactions, 16 to the best of our knowledge, this study of AuPd nanoalloys for propane oxidation under different reaction conditions is the first example of its kind.

The understanding of surface catalytic sites is important for the design of bimetallic nanoalloy catalysts, for which the in situ diffuse reflectance infrared Fourier transform spectroscopy (DRIFTS) technique has proven to be powerful in probing the surface catalytic sites, as shown in our recent study of AuPd on different supports for CO oxidation. 17 While the assynthesized AuPd nanoparticles were under very extensive tensile stress, the thermochemical treatment of the nanoparticles and the type of the support were shown to relieve a significant part of the tensile stress, leading to the random distribution of Au and Pd atoms in the nanoparticles. The formation of intermediate species during propane oxidation and their role in the reaction mechanism are a focal point in studies of Pt or Pd catalysts.18 In a recent DRIFTS study of propane oxidation over Pt/Al<sub>2</sub>O<sub>3</sub>, 19 oxy-carbon species, such as acetate, enolate, aliphatic ester, and acetone, were detected. It was found that an increasing concentration of oxy-carbon species had no effect on CO2 production, indicating that these species are inert spectators during propane oxidation. The intermediate species grow on the Pt/Al<sub>2</sub>O<sub>3</sub> surface and then spill over to the support Al2O3 surface. In another DRIFTS study by Faria et al.20 of Pd/Al2O3/CeO2 for the oxidative stream reforming of propane, it was shown that the formation of formate species (HCOO<sup>-</sup>) is favored over Pd/CeO<sub>2</sub>/ Al<sub>2</sub>O<sub>3</sub> while bicarbonate is detected over Pd/Al<sub>2</sub>O<sub>3</sub>.

While synergistic effects have been shown in previous experimental and theoretical studies of differently-prepared PdAu catalysts in other catalytic reactions, little is known in terms of the roles of metal-support interaction, the bimetal-lic composition and thermochemical processing in terms of

the specific catalyst's phase structures and surface sites. Herein we describe novel findings of an *in situ* DRIFTS study of PdAu nanoalloys with different bimetallic compositions and on different supports in propane oxidation, aiming at understanding the propane oxidation pathways and the catalytic activity in relation to the nanocatalyst's atomic-scale structure and surface-active sites. This understanding is aided by synchrotron X-ray diffraction (XRD) coupled to atomic pair distribution function (PDF) analysis for assessing the nanoalloy's detailed atomic-scale structures.

### 2. Experimental section

### Chemicals

Palladium(II) acetylacetonate (Pd(acac)<sub>2</sub>, 97%), oleylamine (CH<sub>3</sub>(CH<sub>2</sub>)<sub>7</sub>CH=CH(CH<sub>2</sub>)<sub>8</sub>NH<sub>2</sub>, 70%), and borane-morpholine (95%) were purchased from Aldrich. Hydrogen tetrachloroaurate(III) hydrate (HAuCl<sub>4</sub>·xH<sub>2</sub>O, 99.9%) was purchased from Strem Chemicals. Other chemicals such as ethanol, hexane, and isopropanol were purchased from Fisher Scientific. Gases of propane (1 vol% balanced with Ar), H<sub>2</sub> (99.99 vol%), N<sub>2</sub> (99.99 vol%) and O<sub>2</sub> (20 vol% balanced with N<sub>2</sub>) were obtained from Airgas. All chemicals were used as received. TiO<sub>2</sub> was purchased from Acros Organics. Al<sub>2</sub>O<sub>3</sub> was purchased from Alfa Aesar.

#### Synthesis of PdAu nanoparticles

The synthesis of PdAu NPs involved the reduction reaction of two metal precursors. <sup>21</sup> Briefly, palladium(II) acetylacetonate and HAuCl<sub>4</sub>·xH<sub>2</sub>O were dissolved in a desired molar ratio in 15.0 ml oleylamine in a glass vial by heating up to 40 °C and then 1.9 mmol borane morpholine at 75 °C was added under a N<sub>2</sub> atmosphere. The resulting solution was then heated up to 220 °C and kept at this temperature for 30 minutes before cooling down to 70 °C. The NPs were first precipitated out by adding 40 ml isopropanol for centrifugation at 3000 rpm for 20 min and then re-dissolved in a 15 ml hexane and 35 ml ethanol mixture cleaning solvent for centrifugation at 3000 rpm for 30 min. The NPs were redispersed in hexane for further use.

#### Catalyst preparation

The catalysts were prepared from the as-synthesized nanoparticles, including assembling and thermal activation.  $TiO_2$ and  $Al_2O_3$  powder were used as support materials which were mixed with a controlled amount of the as-synthesized nanoparticles followed by sonication and overnight stirring. The product powder was collected and dried under  $N_2$ .

 $TiO_2$ , and  $Al_2O_3$ -supported nanoparticles were activated by thermochemical processing, the details of which were reported previously.<sup>22</sup> Typically, the supported nanoparticles were first treated at 120 °C under  $N_2$  to remove the organic solvent. This was followed by heating at 260 °C under 20%  $O_2$  (balanced with  $N_2$ ) for 1 h to remove the organic capping molecules, and then to 400 °C under 15%  $H_2$  (balanced with  $N_2$ ) for 2 hours to calcine the catalysts. The weight loadings

of the  $TiO_2$  and  $Al_2O_3$  supported PdAu catalysts were around 5% for most of the catalysts studied in this work, which were confirmed by ICP-OES analysis. For example, the metal loading of  $Pd_{31}Au_{69}/Al_2O_3$  was 4.5 wt% whereas that of  $Pd_{31}Au_{69}/TiO_2$  was 5.3 wt%.

#### Catalytic activity measurement

To measure the catalytic activity of supported PdAu catalysts for propane (1 vol% balanced with Ar) + O2 (20 vol% balanced with N2) reaction, a custom-built system was employed, including a temperature-controlled reactor, gas flow/mixing/injection controllers, and an on-line gas chromatograph (Shimadzu GC 8A) equipped with a 5A molecular sieve, Porapak Q packed columns, and a thermal conductivity detector. The catalysts were loaded into a quartz microreactor tube (inner diameter: 4 mm) and wrapped by quartz wool in the middle of the tube (length of the catalyst bed: 6 mm). At a flow rate of 20 ml min<sup>-1</sup>, the system was injected with the feeding gas (0.8 vol% propane +10 vol% O<sub>2</sub>) through the mounted catalyst in the quartz micro reactor. The residence time was about 0.2 seconds. The gas hourly space velocity (GHSV) in the system was around 16 000 h<sup>-1</sup>. Temperature control was achieved using a furnace coupled with a temperature controller. The performances of the catalysts of propane oxidation were determined by analysis of the composition of the tail gas effusing from the quartz micro reactor packed with the catalyst fixed bed using the on-line gas chromatograph.

### Morphology and composition characterization

A transmission electron microscope (TEM) was used to determine the size of the nanoparticles. The nanoparticle samples were suspended in hexane solution and were drop cast onto a carbon-coated copper grid followed by solvent evaporation in an ambient atmosphere.

# High-angle annular dark-field scanning (HAADF-STEM)-energy dispersive spectroscopy (EDS)

HAADF-STEM-EDS was utilized to determine the morphology and map the elemental distribution of the nanoparticles. Following the suspension of the sample in hexane solution, the nanoparticles were drop cast onto a carbon-coated copper grid. The measurements were performed on a JEOL-ARM200F instrument with an acceleration voltage of 200 kV.

# Inductively coupled plasma-optical emission spectroscopy (ICP-OES)

ICP-OES was employed to examine the nanoparticle composition. It was conducted on a PerkinElmer 2000 DV ICP-OES instrument using a cross flow nebulizer with the following parameters: plasma 18.0 L  $Ar_{(g)}$  per min; auxiliary 0.3 L  $Ar_{(g)}$  per min; nebulizer 0.73 L  $Ar_{(g)}$  per min; power 1500 W; peristaltic pump rate 1.40 mL min<sup>-1</sup>. Elements <1.0 mg L<sup>-1</sup> were analyzed using a Meinhardt nebulizer at-

tached to a cyclonic spray chamber to increase the analytical sensitivity with the following parameters: 18.0 L  $Ar_{(g)}$  per min; auxiliary 0.3 L  $Ar_{(g)}$  per min; nebulizer 0.63 L  $Ar_{(g)}$  per min; power 1500 W; peristaltic pump rate 1.00 mL min<sup>-1</sup>.

Ex situ HE-XRD measurements were carried out both on in house equipment and using synchrotron radiation X-rays (E = 80.725 keV) at beamline 1-ID of the Advanced Photon Source at Argonne National Laboratory.

The XRD diffraction data were reduced to the so-called structure factors, S(q), and then Fourier transformed to atomic PDFs G(r), using the relationship

$$G(r) = \frac{2}{\pi} \int_{q=0}^{q_{\text{max}}} q \left[ S(q) - 1 \right] \sin(qr) dq$$
, where  $q_{\text{max}} = 25 \text{ Å}^{-1}$  in the

present experiments. The wave vector q is defined as  $q=4\pi\sin(\theta)/\lambda$ , where  $\theta$  is half of the scattering angle and  $\lambda$  is the wavelength of the X-rays used. Note, as derived, atomic PDFs G(r) are experimental quantities that oscillate around zero and show positive peaks at real space distances r, where the local atomic density  $\rho(r)$  exceeds the average one,  $\rho_o$ . This behavior can be expressed by the equation  $G(r)=4\pi r \rho_o [\rho(\mathbf{r})/\rho_o-1]$ , which is the formal definition of the PDF G(r). Highenergy XRD and atomic PDFs have already proven to be very efficient in studying the atomic-scale structure of nanosized materials. <sup>23,24</sup>

# Diffuse reflectance infrared Fourier transform spectroscopy (DRIFTS)

DRIFTS measurements were performed under propane oxidation reaction conditions on a Bruker Vertex 70 FTIR spectrometer with a MCT detector and a Praying Mantis  $^{\rm TM}$  Diffuse Reflectance Accessory (Harrick Scientific Products, Inc.) Briefly, the sample cup in Praying Mantis TM Diffuse Reflectance Accessory was filled up with 30 mg of PdAu/Al $_2$ O $_3$  catalysts for the propane oxidation reaction at 350 °C. The DRIFT measurements were taken at 64 scans with a resolution of 2 cm $^{-1}$ .

#### Computational modeling

Ab initio calculations were conducted by density functional theory (DFT) utilizing the DMol³ program coming as a part of the Materials Studio program. In the computation, the generalized gradient approximation (GGA) was used. Minimization of energy of all model atomic configurations for unsupported PdAu was carried out. To investigate the interaction between propane, oxygen, intermediate species and the model atomic configurations, the energy of adsorption of propane on the model atomic configurations was measured. It was calculated by  $E_{\rm ads} = -(E_{\rm propane-metal} - E_{\rm metal} - E_{\rm propane})$ , where,  $E_{\rm propane-metal}$ ,  $E_{\rm metal}$  and  $E_{\rm propane}$  are the total energy for the propane-metal complex, the isolated metal configuration, and the isolated propane molecule, respectively.

### 3. Results and discussion

In this section, results from the morphological and structural characterization studies of PdAu nanoparticles are first described to demonstrate the composition controllability and phase structures of the bimetallic nanoparticles. Secondly, the catalytic activities of the catalysts for propane oxidation are discussed in terms of their dependencies on the bimetallic composition and the thermochemical treatment parameters. Finally, the catalytic synergy in correlation with the bimetallic composition and alloying structure is discussed.

### 3.1 Morphology, composition and phase structures

The composition of the PdAu nanoparticles was analyzed using ICP-OES, which revealed a linear relationship between the Au% in the nanoparticles and the Au% in the feeding composition in the synthesis solution (Fig. S1A, ESI†), demonstrating the excellent controllability of the bimetallic composition in the synthesis. There is a slightly lower Au% in the NPs than in the synthesis feeding ratio, indicating that Pd is slightly more favorable in the bimetallic nanoparticles than Au. A set of samples,  $Pd_{91}Au_9$ ,  $Pd_{55}Au_{45}$ , and  $Pd_{31}Au_{69}$  NPs, <sup>17</sup> were examined in this study, which features an average size of 6.5  $\pm$  0.6 nm, 5.5  $\pm$  0.8 nm and 5.3  $\pm$  0.9 nm, respectively (Fig. S1B, ESI†). The NPs were supported on TiO<sub>2</sub> and Al<sub>2</sub>O<sub>3</sub>, and were thermochemically treated to activate the catalysts, yielding an average size of 6.5 nm for all NPs on the support.<sup>25</sup> The morphology and elemental distribution were determined using HAADF-STEM coupled with EDS mapping analysis. Based on the EDS mapping data for the Pd<sub>55</sub>Au<sub>45</sub>/TiO<sub>2</sub> sample (Fig. S1C, ESI†), the distribution of the two metals in the bimetallic NPs is characteristic of a random alloy.

A representative set of X-ray powder diffraction (XRD) patterns for the PdAu/Al<sub>2</sub>O<sub>3</sub> NPs is shown in Fig. 1, featuring a face-centered cubic structure. The diffraction peaks are located between the corresponding Au and Pd peaks, indicating the formation of an alloy structure. The diffraction peak at 38.2° corresponding to Au (111) shifts to a higher diffraction position as Au% decreases, an indication of interatomic distance shortening. For Pd<sub>55</sub>Au<sub>45</sub> nanoparticles, the Bragg peaks are very broad, indicating low crystallinity. The diffraction peaks at 44.3° and 64.5° were assigned to Au (200) and Au (220), respectively. The spectra did not display the signature of oxygen species assigned to PdO at  $2\theta$  of  $33.5^{\circ}$ . This was further confirmed by XPS analysis of the nanoalloys (see Fig. S2, ESI†). The detected peak positions for Pd 3d<sub>3/2</sub> and  $3d_{5/2}$  (~340.2 eV and ~335 eV) were characteristic of the Pd(0) state, and no oxygen species (at 343 eV) were detected.<sup>26</sup> Note that the XRD and XPS data were collected after the catalysts were treated at 260 °C under O2 followed by 400 °C by H2 treatment, in which PdO could be reduced to Pd<sup>0</sup>.

The technique of HE-XRD coupled with PDF was used to examine the atomic-scale alloying phase structure. Fig. 2A displays a set of PDFs for PdAu NPs supported on Al<sub>2</sub>O<sub>3</sub> after thermochemical treatment. The arrangement of sharp peaks in the atomic PDFs represents the presence of well-defined

atomic coordination spheres in PdAu/Al<sub>2</sub>O<sub>3</sub> NPs. The experimental PDFs fit well with the face-centered cubic (fcc) structure model, from which the interatomic distances could be approximated based on lattice parameters. The lattice parameters of PdAu NPs supported on Al2O3 and TiO2 were extracted from the experimental PDF data, which are shown in Fig. 3B. For PdAu/TiO<sub>2</sub>, the lattice parameter increases with increasing Au% in an approximately linear fashion with a slope approaching that predicted by Vegard's law. However, the situation is different for PdAu/Al2O3, which showed a slope smaller than that according to Vegard's law. This finding suggests that the Al<sub>2</sub>O<sub>3</sub> supported PdAu nanoparticles were under very compressive stress.<sup>27</sup> This phenomenon in nanoparticles is due to modification of the electronic properties of the alloy. However, the type of the support appears to relieve a significant part of the compressive stress due to the nature of interaction between the nanoparticle and the support. 17 In comparison with bulk Au (4.079 Å) and bulk Pd (3.891 Å), lattice shrinking has been reported for nanoparticle counterparts on different supports, including Au on TiO2 (3.786 Å), Pd on TiO2  $(3.785 \text{ Å})^{28}$  Au on Al<sub>2</sub>O<sub>3</sub> (4.068 Å), and Pd on Al<sub>2</sub>O<sub>3</sub>  $(3.88 \text{ Å})^{26}$ Note that for a carbon support, lattice expansions were observed, e.g., Au<sub>9</sub>Pd<sub>91</sub>/C (3.941 Å), Au<sub>45</sub>Pd<sub>55</sub>/C (3.982 Å),  $Au_{69}Pd_{31}/C$  (4.015 Å), <sup>17</sup> and Pd/C (3.89 Å) and Au/C (3.93 Å). <sup>29</sup> These subtle differences indicate that the lattice strain characteristics of the nanoparticles are highly dependent on the nanoparticle-support interactions.

The overall lattice shrinking for PdAu/Al<sub>2</sub>O<sub>3</sub> in comparison with PdAu/TiO2 is believed to reflect the difference in metal adhesion on the two different supports. Theoretical studies<sup>30</sup> and experimental data<sup>31</sup> showed that the metal-support interaction strongly depends on the chemical nature of the metal and the support, especially the oxophilicity.32 The adhesion energies of Pd/Al<sub>2</sub>O<sub>3</sub> (4.38 J m<sup>-2</sup>) and Au/Al<sub>2</sub>O<sub>3</sub> (2.31 J m<sup>-2</sup>) have been shown to be higher than those for Pd/TiO<sub>2</sub> (1.092 J m<sup>-2</sup>) and Au/TiO2 (0.292 J m<sup>-2</sup>),33,34 which suggests a stronger metal-support interaction for PdAu/Al<sub>2</sub>O<sub>3</sub> than for PdAu/TiO<sub>2</sub>. The stronger interaction could lead to a smaller contact angle

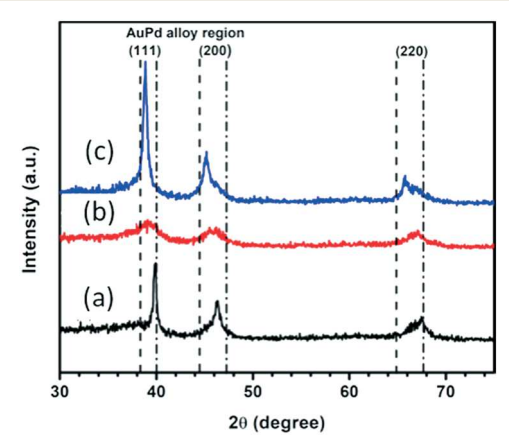


Fig. 1 XRD patterns of NPs: (a)  $Pd_{91}Au_9/Al_2O_3$ , (b)  $Pd_{55}Au_{45}/Al_2O_3$ , and (c) Pd<sub>31</sub>Au<sub>69</sub>/Al<sub>2</sub>O<sub>3</sub> (note that the size of Al<sub>2</sub>O<sub>3</sub> is too fine to display

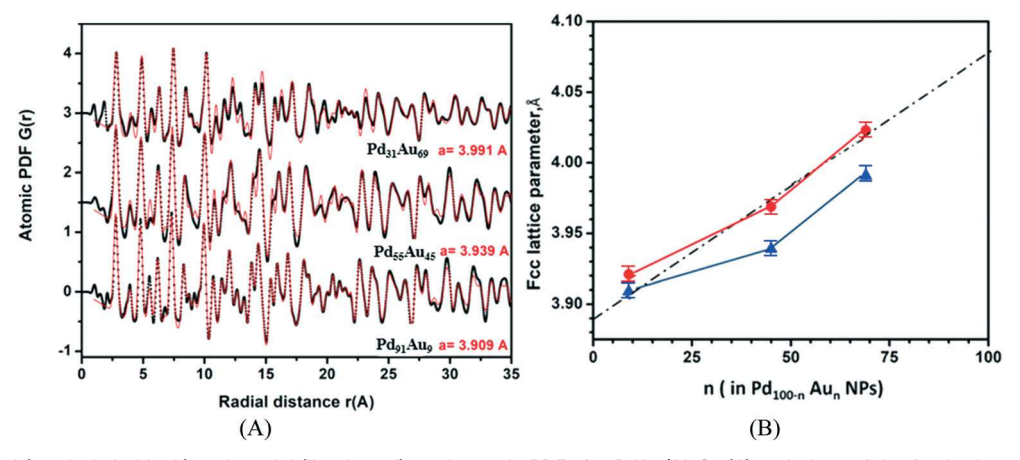


Fig. 2 Experimental (symbols in black) and model (line in red) total atomic PDFs for PdAu/Al<sub>2</sub>O<sub>3</sub> (A) and plots of the fcc lattice parameter of PdAu/ Al<sub>2</sub>O<sub>3</sub> NPs (symbols in blue) and PdAu/TiO<sub>2</sub> (symbols in red) (B), as a function of the relative Au content of the NPs. The broken (dash dot) line represents a 1:1 relationship.

of NPs on the support, under which lattice shrinking could occur. For PdAu/Al<sub>2</sub>O<sub>3</sub> with Au% > 40%, the lattice parameter approaches that for Pd. In comparison, the lattice parameter of PdAu/TiO2 approaches Vegard's law, indicating a better degree of alloying. The strong interaction between PdAu NPs and Al<sub>2</sub>O<sub>3</sub> lead to a partial segregation of Pd<sub>55</sub>Au<sub>45</sub> and Pd<sub>31</sub>Au<sub>69</sub> (Fig. 2B). Another factor affecting the metal segregation is the difference in surface energy, 35 e.g., Pd's surface energy is 2.04 J m<sup>-2</sup> whereas Au's surface energy is 1.62 J m<sup>-2</sup>, which could lead to surface enrichment of Au whereas the nanoparticle core is enriched with Pd. Indeed, EDS mapping data showed that Au atoms in Pd91Au9 tend to segregate toward the NP surface.<sup>17</sup> Moreover, the strong metal-oxide support interaction could also be lowering the sintering rate of NPs, which is important for maintaining the high catalytic activity.<sup>36</sup>

### 3.2 Catalytic oxidation of propane

3.2.1 Catalytic activity. In contrast to the CO oxidation reaction, which is generally believed to follow a Langmuir-Hinshelwood mechanism, i.e., both CO and O2 are activated by co-adsorption, the propane oxidation involves chemisorbed and activated O species reacting with poor adsorption of propane. Since oxygen activation is essential in the catalytic oxidation, the determination of propane oxidation intermediate species provides information for assessing the surface sites on the nanoalloy catalysts.

The measurement of the catalytic activity for propane oxidation focused on PdAu NPs of different compositions supported on TiO2 and Al2O3 supports. Fig. 3 shows a representative set of catalytic data for the as-prepared catalysts (260 °C/O2 treatment followed by 400 °C/H<sub>2</sub> treatment) and the re-oxidized catalysts (260 °C/O<sub>2</sub> treatment of the as-prepared catalysts). First, the catalytic activity depends on the bimetallic composition and the chemical nature of the support, exhibiting the order of Pd<sub>55</sub>Au<sub>45</sub> > Pd<sub>91</sub>Au<sub>9</sub> > Pd<sub>31</sub>Au<sub>69</sub>, for both TiO<sub>2</sub> and Al<sub>2</sub>O<sub>3</sub> supported catalysts (Fig. 3A and B). Secondly, the overall catalytic activity was found to be almost independent of the O2 treatment (260 °C/ O2) for most of the catalysts, except for Pd91Au9/Al2O3 which showed a subtle increase after the O2 treatment. This finding is

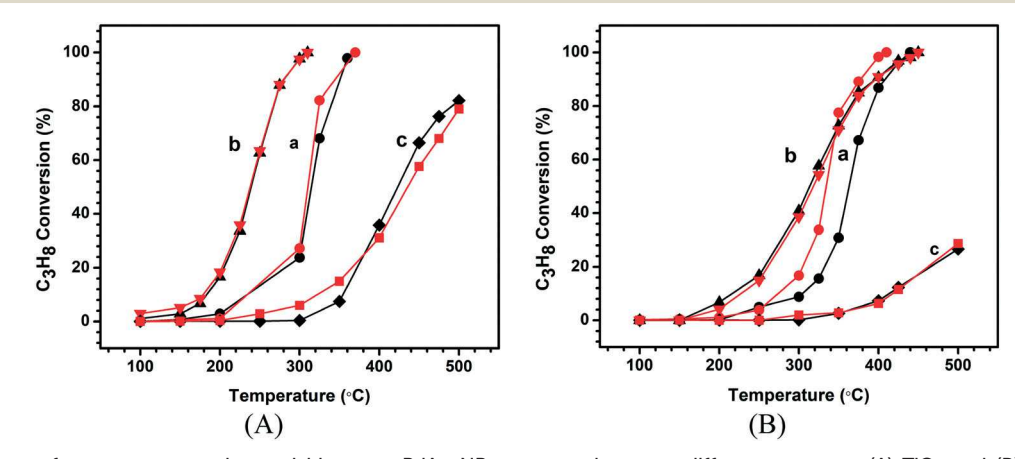


Fig. 3 Comparisons of propane conversion activities over PdAu NPs supported on two different supports: (A) TiO<sub>2</sub> and (B) Al<sub>2</sub>O<sub>3</sub>. Pd<sub>91</sub>Au<sub>9</sub> (a, circle); Pd<sub>55</sub>Au<sub>45</sub> (b, triangle); Pd<sub>31</sub>Au<sub>69</sub> (c, square). Catalyst treatments: (1) as-prepared catalysts (260 °C/O<sub>2</sub> treatment followed by 400 °C/H<sub>2</sub> treatment, black); 2) 260 °C/O2 re-treated catalysts (red).

in contrast to data for Pd alloyed with base transition metals where oxophilicity has a strong impact on catalytic activity.<sup>37</sup> Note that the catalytic data of commercial Au/TiO2 show very low activity in comparison with the binary PdAu catalyst (see Fig. S5A, ESI†). The PdAu/TiO2 catalysts clearly show an enhanced catalytic activity, e.g., Pd<sub>55</sub>Au<sub>45</sub>/TiO<sub>2</sub> which has values of  $T_{10}$  = 190 °C and  $T_{50}$  = 220 °C (see Fig. 4A and B) in comparison with values of  $T_{10}$  = 290 °C and  $T_{50}$  = 350 °C previously reported for 2 wt% Pd/TiO2.38 For Pd55Au45/Al2O3, an enhanced activity was also observed, but the catalytic activities in comparison with Pd/Al<sub>2</sub>O<sub>3</sub> depend on the preparation methods of the catalysts. Examples of the activities reported for Pd/Al<sub>2</sub>O<sub>3</sub> include  $T_{10} = 320$  °C and  $T_{50} = 390$  °C, <sup>39</sup> and  $T_{10} = 240$  °C and  $T_{50} = 320$  $^{\circ}$ C.  $^{40}$  For commercial 5 wt% Pd/Al $_{2}$ O $_{3}$ ,  $T_{10}$  = 225  $^{\circ}$ C and  $T_{50}$  = 290 °C (see Fig. S5B, ESI†). Again, the comparison was limited at this point because it was affected by the differences in particle sizes and catalyst preparation methods.

By comparison of the catalytic activities in terms of the oxidation temperatures (Fig. 3), a maximum catalytic activity is revealed for the catalysts with a Pd:Au ratio of 1:1. Interestingly, a close examination of the data in Fig. 3 indicates subtle differences in terms of the relative  $T_{10}$ ,  $T_{50}$  and  $T_{75}$  values for the catalysts before and after the oxidative thermochemical treatment for  $Pd_nAu_{100-n}/TiO_2(I)$  and  $Pd_{100-n}Au_n/Al_2O_3(II)$  (Fig. 4). Note that for  $Pd_{31}Au_{69}/Al_2O_3(II)$ both  $T_{50}$  and  $T_{75}$  fall above the temperature range because of its low activity. For Pd<sub>100-n</sub>Au<sub>n</sub>/TiO<sub>2</sub>(1), while there were small changes in most cases for <50% Au or >50% Au, little change was observed for ~50% Au before and after the oxidative thermochemical treatment. Similar results were also obtained for  $Pd_{100-n}Au_n/Al_2O_3(II)$  with <50% Au and ~50% Au. These observations are remarkable, suggesting not only the operation of a composition-dependent catalytic synergy, especially for the PdAu NPs with ~50% Au. Note that the present work focused on studying the composition-activity dependence of the supported PdAu nanoparticles in the propane reaction in terms of intermediates in relation to catalytic activity. There is a need to understand the stability and it would involve testing the catalysts in different gas mixtures and temperatures or different ageing conditions. There is also a need to compare the stabilities of AuPd and Pd catalysts. Our preliminary work under very limited conditions showed an indication of higher activity and stability for a certain AuPd catalyst, but the confirmation, especially in comparison with Pd catalysts under the same or comparable particle sizes and by similar preparation methods, will be provided by future work.

In order to understand the mechanistic details, the kinetic data were examined, revealing two different  $E_a$  values for low and high reaction temperature ranges (see Fig. S3, ESI†). The overall  $E_a$  value is higher in the low temperature range (100 to 270 °C) than in the high temperature range (300 to 500 °C). Secondly, Ea exhibits a minimum at a Pd:Au ratio of  $\sim$ 50:50, consistent with the reaction temperature data. The overall  $E_a$  values in the low temperature range for the catalysts are slightly lower than those reported for the catalytic oxidation of propane (60-90 kJ mol<sup>-1</sup>). In addition to the dependence of  $E_a$  on the bimetallic composition, a clear dependence on the thermal treatment condition was also revealed. In the low temperature range (Fig. S4A, ESI†), the activation energy was increased after O2 treatment for PdnAu100-n/TiO2 with n < 50. This is consistent with the measured  $T_{10}$  values. (see Fig. 4A). However, the activation energy for n < 50dropped in the case of Al<sub>2</sub>O<sub>3</sub> supported Pd<sub>n</sub>Au<sub>100-n</sub> (see Fig. S4C, ESI†). For n smaller than 50 (e.g.,  $Pd_{31}Au_{69}/TiO_2$ ), the activation energy showed a decrease after O2 treatment. This is also consistent with the  $T_{10}$  values (see Fig. 4A). Note that the activation energy remained unchanged after O2 treatment for  $n \sim 50$  which is consistent with the measured  $T_{50}$  values (see Fig. 4B). In the high temperature range (Fig. S4B and S4D, ESI†), the activation energy showed an increase for n < 50and an increase for n > 50 after  $O_2$  treatment, which is consistent with the trend of  $T_{75}$  values (see Fig. 4C).

Taken together, the kinetic results suggest switching-type catalytic activities in terms of lower and higher  $T_{10}$  and  $T_{75}$  values in the low and high reaction temperature ranges, as shown in Fig. 4A and C, in terms of the oxidative treatment. The fact that the increase in  $E_{\rm a}$  for the oxidized  ${\rm Pd}_n{\rm Au}_{100-n}/{\rm Pd}_n{\rm$ 

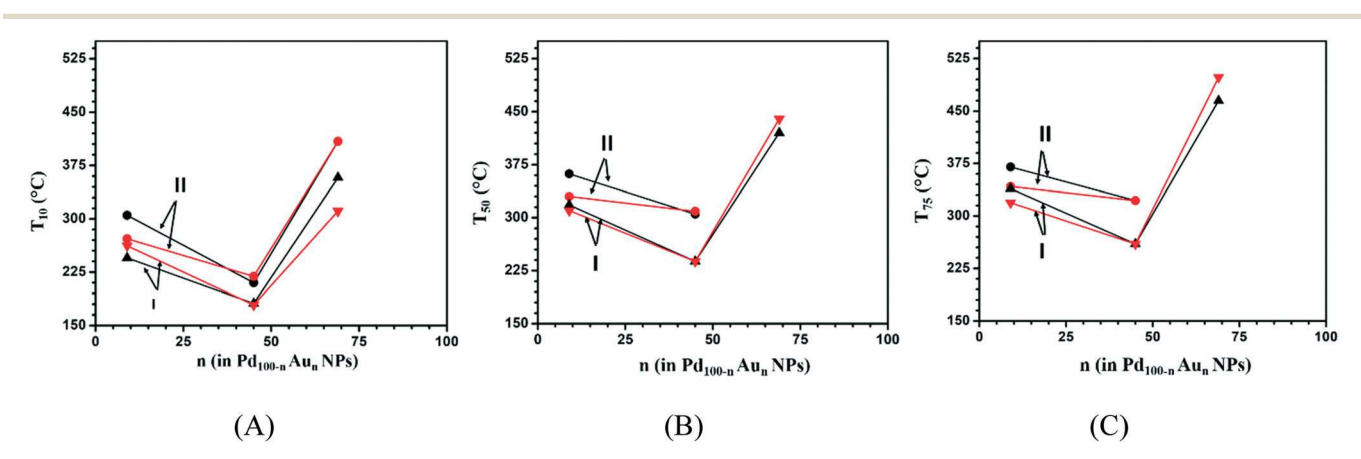


Fig. 4 Plots of  $T_{10}$  (A),  $T_{50}$  (B), and  $T_{75}$  (C) values vs. bimetallic composition for propane oxidation over  $Pd_{100-n}Au_n/TiO_2$  (I, triangles) and over  $Pd_{100-n}Au_n/Al_2O_3$  (II, circles) catalysts for the fresh catalysts (black) and the one treated under  $O_2$  at 260 °C for 30 min (red).

 $TiO_2$  catalysts for n < 50 did not change the conversion activity is indicative of the immunity of both Au and Pd from oxidation in the nanoalloy under the reaction conditions. The finding that PdAu/TiO2 exhibits an activity higher than that for PdAu/Al<sub>2</sub>O<sub>3</sub> is believed to reflect a combination of the higher degree of alloving in the NPs and the higher oxygen capability for TiO2. For PdAu/Al2O3, in which the compressive stress is at a maximum (Fig. 2B), a down shift of the d-band level with respect to the Fermi level<sup>41</sup> could reduce the binding energy of propane or intermediate species and enhance the oxidation.

3.2.2. In situ DRIFTS characterization. TiO2 is known for its active lattice oxygen, 42 leading to a high oxygen capacity. PdAu/Al<sub>2</sub>O<sub>3</sub>, while showing an activity lower than PdAu/TiO<sub>2</sub>, exhibited a composition dependence of activity similar to PdAu/TiO2. There is also a significant lattice shrinking for Au% > 40% in comparison with the fully-alloyed character of PdAu/TiO<sub>2</sub>. In this work, the Al<sub>2</sub>O<sub>3</sub> support was used as an example for studying the catalytic synergy of AuPd NPs in propane oxidation. In comparison with TiO2, Al2O3 is known for its strong interaction with noble metals and exhibition of high resistance for nanoparticle aggregation especially at high reaction temperature which is required for oxidation of hydrocarbons such as propane.43 Based on these observations, an in situ DRIFTs study was performed for propane oxidation over PdAu/Al<sub>2</sub>O<sub>3</sub> catalysts in an attempt to determine the correlation among the nanostructure, the activity, and the surface species. Surface species over PdAu /Al<sub>2</sub>O<sub>3</sub> catalysts were monitored by DRIFTS during propane oxidation at 350 °C under a flow rate of 80 mL min<sup>-1</sup> with an O<sub>2</sub>/C<sub>3</sub>H<sub>8</sub> ratio of 5:1. Fig. 5 represents a typical set of DRIFTS spectra monitoring the surface species during propane oxidation over different compositions of PdAu/Al<sub>2</sub>O<sub>3</sub>. The observed peaks depend on the bimetallic composition in terms of the peak position and intensity. As the reaction progresses, the intensities of the bands become stronger in the case of Pd<sub>91</sub>Au<sub>9</sub> (Fig. 5A) and in Pd<sub>55</sub>Au<sub>45</sub> (Fig. 5B). However, the peak intensity is much weaker for  $Pd_{31}Au_{69}$  (Fig. 5C). The peak at ~2970 cm<sup>-1</sup> is assigned to alkane C-H vibration bonds of gaseous propane, while bands at around 2902 cm<sup>-1</sup> are attributed to CH<sub>2</sub>(ads) and CH<sub>3</sub>(ads) species.<sup>20</sup> The bands observed in the range ~2340-2360 cm<sup>-1</sup> are characteristic of gaseous CO<sub>2</sub>.<sup>44</sup> Note that the spectra did not display the signature of adsorbed CO species in the range of around 2200 to 2400 cm<sup>-1</sup>.<sup>45</sup> Major peaks in the range of ~1730-1330 cm<sup>-1</sup> were clearly detected over Pd55Au45 and Pd91Au9, part of which were weak but observable over Pd31Au69. Note that the catalytic activity measurement was conducted in a packed quartz reactor, whereas the DRIFTs cell was an open reactor. The difference in the experimental set-ups could result in different gas compositions, flow rates and GHSVs between these two measurements, but our analysis of the DRIFTS data in this work mainly focused on the identification of the surface species, rather than a detailed correlation with their reaction kinetics.

The evolution of oxy-carbon bands is examined in detail in the range of 1730-1330 cm<sup>-1</sup> (Fig. 5 right panel). Detailed

peak assignments are shown in Table S1, ESI.† The peaks detected at 1560 and 1455 cm<sup>-1</sup> (Fig. 5A right) and at 1580 and 1460 cm<sup>-1</sup> (Fig. 5B right) are assigned to adsorbed acetate species. 46,47 The bands at 1683 cm<sup>-1</sup> (Fig. 5A right) and 1681 cm<sup>-1</sup> (Fig. 5B right) are assigned to adsorbed acetone species. 48 The shoulder bands at 1730-1733 cm<sup>-1</sup> (Fig. 5A and B) are assigned to adsorbed carbonyl groups with an aliphatic ester group. 49,50 The band at 1645 cm<sup>-1</sup> is assigned to adsorbed bicarbonate species (Fig. 5A and B). 51,52 The band at 1593 cm<sup>-1</sup> is consistent with the absorption of formate species (Fig. 5A). <sup>53,54</sup> The peak at 1470 cm<sup>-1</sup> (Fig. 5A) is attributed to adsorbed methoxy groups. 55-57

Propane oxidation over a commercial Pd/Al<sub>2</sub>O<sub>3</sub> catalyst was also examined by in situ DIRFTs to probe the surface species during propane oxidation. The reaction temperature was slightly different. Fig. S6 in the ESI† shows a representative set of DRIFTS spectra. As shown in (Fig. S6, ESI†), there are four major peaks observed for Pd/Al2O3. The peaks at 1585 and 1470 cm<sup>-1</sup> are characteristic of adsorbed acetate species. The band at 1675 cm<sup>-1</sup> is assigned to adsorption of acetone. The shoulder band at 1730 cm<sup>-1</sup> is assigned to carbonyl groups with an aliphatic ester group. In comparison with PdAu, the peaks of acetate over Pd/Al<sub>2</sub>O<sub>3</sub> were detected at higher wavenumbers and they were observable over Pd<sub>55</sub>Au<sub>45</sub>/ Al<sub>2</sub>O<sub>3</sub> and Pd<sub>91</sub>Au<sub>9</sub>/Al<sub>2</sub>O<sub>3</sub> only. The peaks of acetone species were found for Pd<sub>91</sub>Au<sub>9</sub>/Al<sub>2</sub>O<sub>3</sub> and Pd<sub>55</sub>Au<sub>45</sub>/Al<sub>2</sub>O<sub>3</sub> only. Similarly, the peaks for the aliphatic ester were only observable for Pd<sub>55</sub>Au<sub>45</sub>/Al<sub>2</sub>O<sub>3</sub> and Pd<sub>91</sub>Au<sub>9</sub>/Al<sub>2</sub>O<sub>3</sub>.

It is evident that oxy-carbon species (COO, OCO, CCO, etc.) were observed on these catalysts during the propane oxidation reaction. The subtle differences in terms of the changes in peak intensities for the catalysts with different bimetallic compositions were further analyzed to assess the formation of different intermediate species during the oxidation reaction. Fig. 6A and B show the transient plots of peak intensities for diagnostic bands, including aliphatic ester  $v(CH_3C(=O)-O) \sim 1730 \text{ cm}^{-1}$ , acetone  $v((CH_3)_2C=O) \sim 1681$ cm<sup>-1</sup>, bicarbonate  $v_{as}(HOCO_2^-)$  ~1644 cm<sup>-1</sup>, formate  $v_{as}(HCOO^{-}) \sim 1593 \text{ cm}^{-1}$ , and acetate  $v_{as}(CH_3CO_2^{-}) \sim 1560$ cm<sup>-1</sup>, displaying subtle differences. There is a clear increase in the oxy-carbon species as the reaction progresses for Pd<sub>91</sub>Au<sub>9</sub>/ Al<sub>2</sub>O<sub>3</sub> and Pd<sub>55</sub>Au<sub>45</sub>/Al<sub>2</sub>O<sub>3</sub> while the change is insignificant in the case of Pd<sub>31</sub>Au<sub>69</sub>/Al<sub>2</sub>O<sub>3</sub> (see Fig. S7, ESI†). Interestingly, for Pd<sub>55</sub>Au<sub>45</sub>/Al<sub>2</sub>O<sub>3</sub> the growth rate of the peak intensity for the adsorbed acetate species  $(v_{as}(CH_3CO_2^-) \sim 1560 \text{ cm}^{-1})$  is much greater than that for the adsorbed aliphatic ester, acetone and bicarbonate species. For Pd<sub>91</sub>Au<sub>9</sub>/Al<sub>2</sub>O<sub>3</sub>, the growth rate for bicarbonate and formate species is slightly greater than that for the acetate, acetone, and ester species.

If first-order reactions are considered for the adsorption and desorption of the intermediate species, i.e.,

$$R \xrightarrow{k_1} I_{ads} \xrightarrow{k_2} P \tag{1}$$

we would have the following type of equation for the surface coverage ( $\theta$ : coverage of intermediate species,  $A_{ids}$ ) vs. time:

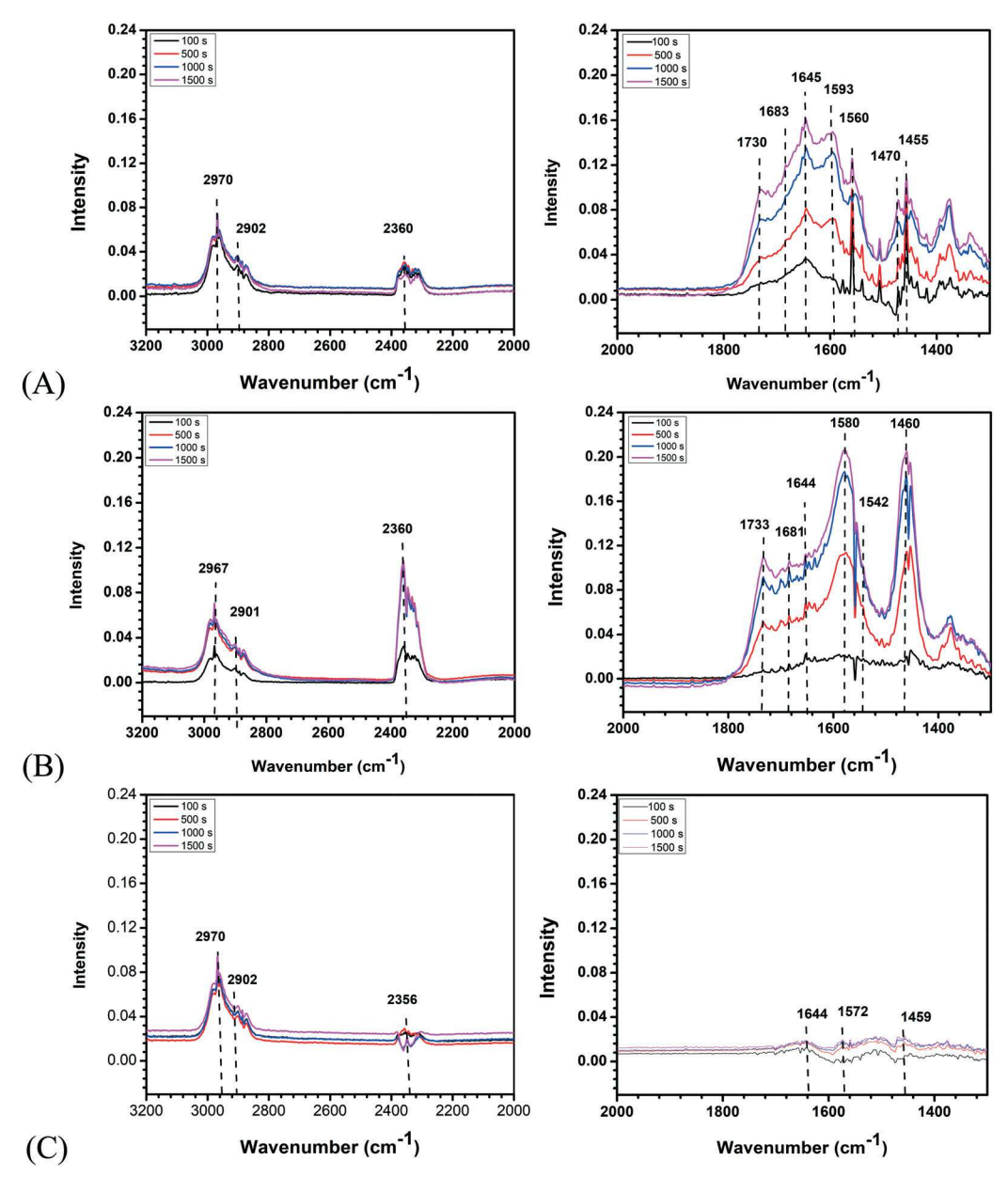


Fig. 5 In situ DRIFTS spectra recorded during propane oxidation over  $Pd_{91}Au_9/Al_2O_3$  (A),  $Pd_{55}Au_{45}/Al_2O_3$  (B), and  $Pd_{31}Au_{69}/Al_2O_3$  (C) at 350 °C; the spectra on the right are zoomed-in views of the spectra in the 1300–2000 cm<sup>-1</sup> region.

$$\theta = \left(\frac{k_1}{k_1 - k_2}\right) \left(\exp\left(-k_2 t\right) - \exp\left(-k_1 t\right)\right) \tag{2}$$

By applying the above equation to the data in Fig. 6 in terms of peak intensity, we obtain the values of the apparent rate constants ( $k_1$  and  $k_2$ ) (see Table S2†). In general, the apparent rate constant is higher for the species showing a higher intensity (e.g., acetate  $2.71 \times 10^{-4}$ ,  $Pd_{55}Au_{45}$ ) than for those with a lower intensity (e.g., ester  $1.38 \times 10^{-4}$ ,  $Pd_{55}Au_{45}$ ). Interestingly,  $k_2$  (e.g., bicarbonate  $9.61 \times 10^{-4}$ ,  $Pd_{91}Au_9$ ) is higher than  $k_1$  (e.g., bicarbonate  $2.22 \times 10^{-4}$ ,  $Pd_{91}Au_9$ ) for all the intermediate species detected. The subtle differences in the apparent rate constants among the catalysts with differ-

ent compositions are believed to reflect that the formation, desorption or further oxidation of intermediate species depends strongly on the surface active sites.

Fig. 7 compares the peak intensities for the oxy-carbon species identified in the range of 1730–1330 cm $^{-1}$  for  $Pd_{91}Au_{9}/Al_{2}O_{3}$ ,  $Pd_{55}Au_{45}/Al_{2}O_{3}$ , and  $Pd_{31}Au_{69}/Al_{2}O_{3}$ . It is clear that the acetate species is maximized over  $Pd_{55}Au_{45}/Al_{2}O_{3}$  whereas the bicarbonate species is maximized over  $Pd_{91}Au_{9}/Al_{2}O_{3}$ , and  $Pd_{55}Au_{45}/Al_{2}O_{3}$ , a key difference is that while the growth rate for acetate species is greater for  $Pd_{55}Au_{45}/Al_{2}O_{3}$ , the growth rate for bicarbonate and formate species is greater for  $Pd_{91}Au_{9}/Al_{2}O_{3}$ , the latter of which also showed the extra ester species. This finding demonstrates that the chemical or intermediate species are

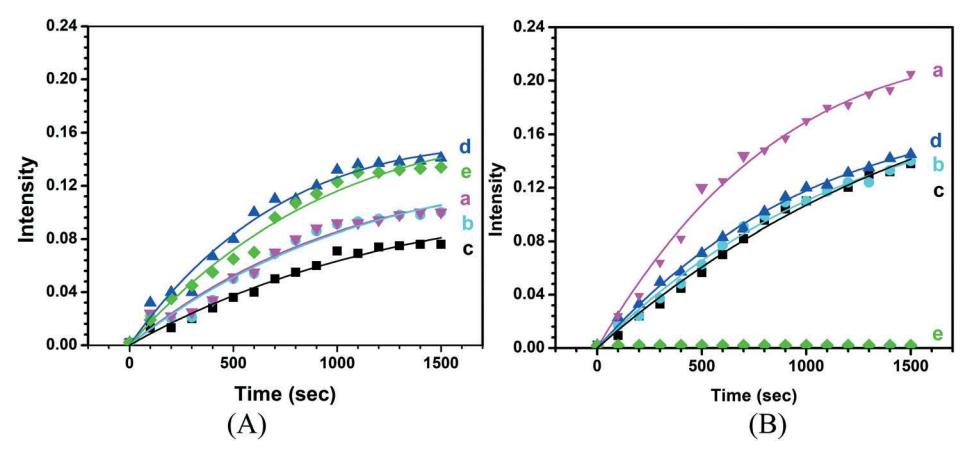


Fig. 6 (A and B) plots of peak intensity (peak height) vs. time for propane oxidation adsorption at 350 °C for several major bands detected, including acetate  $v_{as}(CH_3CO_2^-) \sim 1560$  cm<sup>-1</sup> (a, pink), acetone  $v(CH_3)_2C=0 \sim 1681$  cm<sup>-1</sup> (b, cyan), aliphatic ester  $v(CH_3C(=0)-0) \sim 1730$  cm<sup>-1</sup> (c, black), bicarbonate  $v_{as}(HOCO_2^-) \sim 1644 \text{ cm}^{-1}$  (d, blue), and formate  $v_{as}(HCOO^-) \sim 1593 \text{ cm}^{-1}$  (e, green), for  $Pd_{91}Au_9/Al_2O_3$  (A) and  $Pd_{55}Au_{45}/Al_2O_3$ (B); the data were extracted from Fig. 6. The fitting curve was based on eqn (1). See Table S4 $\dagger$  for the calculated  $k_1$  and  $k_2$ .

strongly dependent on the bimetallic composition. For Pd<sub>31</sub>Au<sub>69</sub>/Al<sub>2</sub>O<sub>3</sub>, the peak intensities are much smaller than those for the Pd<sub>91</sub>Au<sub>9</sub>/Al<sub>2</sub>O<sub>3</sub> and Pd<sub>55</sub>Au<sub>45</sub>/Al<sub>2</sub>O<sub>3</sub>.

In Fig. 7, the DRIFTS peak intensities of the major intermediate species detected in propane oxidation at 350 °C over the PdAu catalysts of three different compositions intermediate species are arranged from non or 1st C-C bond cleaved oxidation species (acetone, ester, and acetate, i.e., group-I) to 1st and 2nd C-C bond cleaved oxidation species (formate, bicarbonate, i.e., group-II). In comparison with the experimentally observed maximum activity for the catalyst with Pd: Au ~50 (see Fig. 4A and B) for propane oxidation, the catalyst composition dependence of the detected intensities for group-I species seems to correlate well in terms of the relative amount of surface species. For group-II species, in comparison with the relatively high levels of surface species for Pd91Au9, the absence of formate species and the reduced level of bicarbonate species for propane oxidation using Pd<sub>55</sub>Au<sub>45</sub> are evident, suggesting the effective conversion of group-II species to CO2. There exist different possibilities for the absence of formate species. By comparing the results for PdAu catalysts with different compositions, we were able to assess the possibilities of different reaction pathways, but our assessments were largely linked to the dependences of group I or II species on the bimetallic composition. In other words, this result correlates to a certain degree with the higher catalytic activity Pd<sub>55</sub>Au<sub>45</sub>. Since there is essentially no or very low activity for the Au-rich catalyst (Pd31Au69), the detected group-I and -II species are essentially zero or very small.

### 3.3 Catalytic synergy in terms of composition-structureactivity correlation

The results shown in Fig. 7 provided the relative abundances of the peaks associated with the chemical and intermediate species being detected for us to assess the relative amounts of the none or 1st C-C bond cleaved oxidation species (acetone, ester, and acetate, i.e., group-I) to 1st and 2nd C-C bond cleaved oxidation species (formate, bicarbonate, i.e., group-II). For pure Pd and Pd-rich Pd91Au9, while the activity for C-H and first C-C bond cleavages is comparable to that for Pd<sub>55</sub>Au<sub>45</sub>, the cleavage of the second C-C bonds appears to be less effective (see Scheme 1). Therefore, there is a synergy for the catalytic activity of propane oxidation over Pd<sub>55</sub>Au<sub>45</sub>, showing activity enhancement by the introduction of an appropriate level of Au into the Pd alloy.

In contrast to the absence of or almost no intermediate species detected on Au-rich alloys (i.e., Pd<sub>31</sub>Au<sub>69</sub>/Al<sub>2</sub>O<sub>3</sub>), formate and bicarbonate were detected on Pd-rich and Pd  $\sim$ 50% alloys (i.e., Pd<sub>91</sub>Au<sub>9</sub>/Al<sub>2</sub>O<sub>3</sub> and Pd<sub>55</sub>Au<sub>45</sub>/Al<sub>2</sub>O<sub>3</sub>), which is consistent with the high catalytic activities of both catalysts.

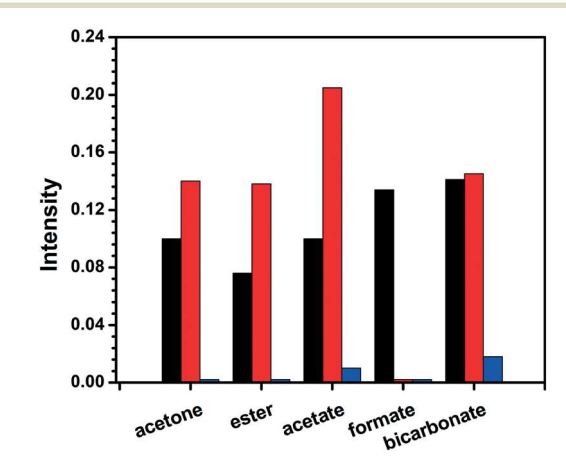


Fig. 7 Comparison of the DRIFTS peak intensities for some of the major intermediate species detected in propane oxidation at 350 °C over Pd<sub>91</sub>Au<sub>9</sub>/Al<sub>2</sub>O<sub>3</sub> (black bars), Pd<sub>55</sub>Au<sub>45</sub>/Al<sub>2</sub>O<sub>3</sub> (red bars), and Pd<sub>31</sub>Au<sub>69</sub>/Al<sub>2</sub>O<sub>3</sub> (blue bars) catalysts. The intermediate species are arranged from none surface species, to 1st C-C bond cleaved oxidation species (acetone, ester, and acetate), and to complete C-C bond cleaved oxidation species (formate, and bicarbonate).

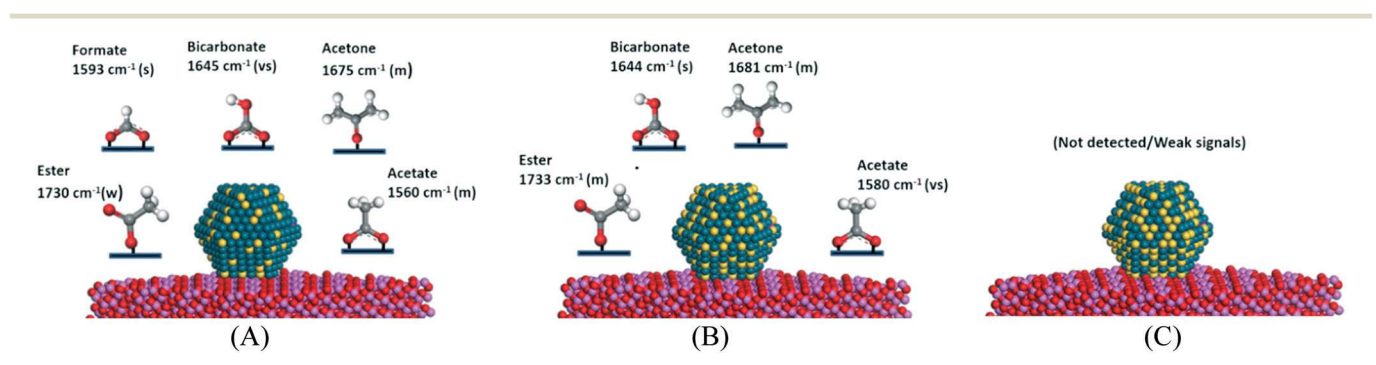
However, in comparison with Pd<sub>91</sub>Au<sub>9</sub>/Al<sub>2</sub>O<sub>3</sub>, formate was not detected and the intensity of bicarbonate species was reduced for propane oxidation over Pd<sub>55</sub>Au<sub>45</sub>/Al<sub>2</sub>O<sub>3</sub>, indicating that the complete C-C cleaved products were likely released as CO2. This finding is consistent with the higher activity of Pd<sub>55</sub>Au<sub>45</sub>/Al<sub>2</sub>O<sub>3</sub> than Pd<sub>91</sub>Au<sub>9</sub>/Al<sub>2</sub>O<sub>3</sub> (see activity data in Fig. 4). Since the propensity of oxidation of Au is much lower, the surface oxophilicity of Pd<sub>91</sub>Au<sub>9</sub>/Al<sub>2</sub>O<sub>3</sub> is likely to be higher than Pd<sub>55</sub>Au<sub>45</sub>/Al<sub>2</sub>O<sub>3</sub>, which explains the difference in terms of retaining the adsorbed intermediate formate and bicarbonate species between the two catalysts. This difference in oxophilicity is also manifested by the lattice difference between these two catalysts, i.e., the less oxophilic PdAu/Al<sub>2</sub>O<sub>3</sub> showed more significant lattice shrinking (see Fig. 2). The general correlation of oxophilicity to the lattice shrinking has been established in our previous studies<sup>58,59</sup> for different nobletransition metal nanoparticles, indicating that the lattice expands and contracts upon being treated in oxidizing (O2) and reducing (H<sub>2</sub>) atmospheres, respectively. We believe that a different support could also influence the overall oxophilicity of the AuPd catalysts.

For catalytic propane oxidation, oxygen activation is believed to play a major role in achieving the synergistic enhancement of the activity at  $n \sim 50$ . Since Au exhibits immunity from oxidation in the nanoalloy under the reaction conditions, it is possible that Au plays an important role in tuning surface sites but also the surface oxophilicity of Pd under the reaction temperature. In a study of CO oxidation over PdAu (synthesized using an ~1:1 feeding ratio)/Al<sub>2</sub>O<sub>3</sub> at 205 °C using combined XAFS/DRIFT measurements, 60 it was revealed that the stronger binding of CO on Pd atoms than Au lead to the formation of a Pd shell and a Au core. In another study of Au<sub>88</sub>Pd<sub>12</sub>/TiO<sub>2</sub> in the presence of CO/O<sub>2</sub> under reaction conditions,61 a similar core-shell evolution was also observed, leading to rapid deactivation of the catalyst. For propane oxidation, no apparent deactivation for our AuPd catalysts at  $\sim T_{50}$  was observed even after extensive thermochemical treatment under oxygen, especially for Au% ≤ 50. Based on our previous report, <sup>17</sup> we believe that coreshell evolution was insignificant. This assessment is supported by the data for the high- and medium-Pd catalysts (Au  $\leq$  50) in the reaction temperature range (Fig. 4A and B and S3A, ESI†). For Au% > 50 and under reaction temperatures above  $T_{50}$ , there may be a slight enrichment of Pd as a result of the diffusion from the Pd-rich core, which is consistent with the data for the low-Pd catalyst (Au% > 50) in the high temperature range (Fig. 4C and S4B, ESI†). In a study<sup>62</sup> of the reaction pathway of propane oxidation over Pt/Al<sub>2</sub>O<sub>3</sub>, the existence of SO<sub>4</sub><sup>2-</sup> was found to facilitate the breaking of carbon-carbon bonds causing alteration of the reaction pathway. In the DRIFTS study of the catalytic oxidative stream of propane Pd/Al<sub>2</sub>O<sub>3</sub> and Pt/CeO<sub>2</sub>/Al<sub>2</sub>O<sub>3</sub>, wo main species were identified, formate species (1390 and 1590 cm<sup>-1</sup>) and monodentated carbonate species (1502 cm<sup>-1</sup>); the formate is active on Pd/Al<sub>2</sub>O<sub>3</sub> while the carbonate is active on Pd/CeO<sub>2</sub>/Al<sub>2</sub>O<sub>3</sub>. In comparison, our detection of higher amounts of carbonate and formate species for the Pd-rich alloy (Pd<sub>9</sub>Au<sub>91</sub>/Al<sub>2</sub>O<sub>3</sub>) seems to reflect a combination of the activities of Pd/Al<sub>2</sub>O<sub>3</sub> and Pd/CeO<sub>2</sub>/Al<sub>2</sub>O<sub>3</sub>. The propane oxidation reaction mechanism depends strongly on the chemical nature of the metal and support, as well as additives.20,63

By analysis of the distribution of intermediate species among Pd<sub>91</sub>Au<sub>9</sub>/Al<sub>2</sub>O<sub>3</sub>, Pd<sub>55</sub>Au<sub>45</sub>/Al<sub>2</sub>O<sub>3</sub>, and Pd<sub>31</sub>Au<sub>69</sub>/Al<sub>2</sub>O<sub>3</sub> catalysts during propane reaction, there are clearly subtle differences in terms of the number of chemical or intermediate species and their diagnostic peak positions. For example, bicarbonate and acetate species were detected over Pd91Au9/ Al<sub>2</sub>O<sub>3</sub> and Pd<sub>55</sub>Au<sub>45</sub>/Al<sub>2</sub>O<sub>3</sub> but not over Pd<sub>31</sub>Au<sub>69</sub>/Al<sub>2</sub>O<sub>3</sub>. Ester species were detected over Pd91Au9/Al2O3 but not over Pd<sub>55</sub>Au<sub>45</sub>/Al<sub>2</sub>O<sub>3</sub>. Based on the reaction steps proposed earlier for propane oxidation over Pd/Al<sub>2</sub>O<sub>3</sub>, 20 some of the hypothesized reaction steps are considered for assessing the detection of the intermediate species:

- (1) Initial C-H bond cleavage by reacting with adsorbed O species followed by adsorption of  $C_3H_{(8-n)}$  (n = 1, 2, ...)
  - e.g.,  $C_3H_8 + O_{ads.}$  (on Pd site)  $\rightarrow C_3H_{(8-n)}$  (ads.)  $+ H_2O$  (ads)
- (2) Reaction of activated C<sub>3</sub>H<sub>(8-n)</sub> species with activated O species leading to cleavages of the first C-C bond and additional C-H bonds to form intermediate species.

e.g.,  $C_3H_{(8-n)}$  (ads.) + O (ads)  $\rightarrow$  intermediate species (e.g., ester, acetate, acetone, etc.)



Scheme 1 Illustrations of the major intermediate species detected for propane oxidation over Pd<sub>91</sub>Au<sub>9</sub>/Al<sub>2</sub>O<sub>3</sub> (A), Pd<sub>55</sub>Au<sub>45</sub>/Al<sub>2</sub>O<sub>3</sub> (B), and Pd<sub>31</sub>Au<sub>69</sub>/Al<sub>2</sub>O<sub>3</sub> (C). Atomic color codes: Pd (green), Au (yellow), C (gray), H (white), O (red), and Al (pink). (vs: very strong; s: strong; m: medium; w: weak; and vw: very weak).

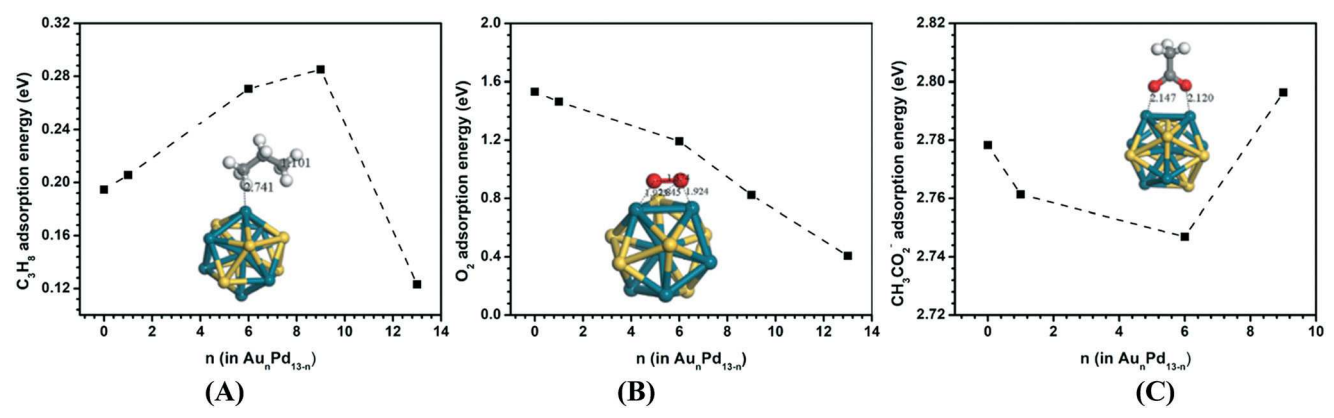


Fig. 8 DFT calculated adsorption energy for molecularly adsorbed propane (A), molecularly adsorbed oxygen (B), and adsorbed acetate (C) on  $Pd_{13-n}Au_n$  clusters of different n values. Inserts: Snapshots of the surface adsorption and cluster models.

(3) Reaction of the first-C-C bond cleaved intermediate species with activated O species leading to cleavages of the second C-C bond and additional C-H bonds to form intermediate species

e.g., first-C-C bond cleaved intermediate species (e.g., ester, acetate, acetone, etc.) + O (ads)  $\rightarrow$  both C-C bond cleaved intermediate species (e.g., bicarbonate, formate, etc.).

(4) Decomposition and release of the adsorbed intermediate species as CO<sub>2</sub> and H<sub>2</sub>O.

Intermediate species  $\rightarrow CO_2 + H_2O$ .

Based on previous reports, <sup>16,18,60</sup> C-H cleavage occurs with activated oxygen on a catalyst surface from the oxygen feed or provided by the support (steps in (1)), which was considered to be the rate determining step for propane oxidation. <sup>64</sup> Following the hydrocarbon cracking, the hydrocarbon fragments react with activated oxygen species, forming first-C-C bond cleaved intermediate species (ester, acetate, acetone, *etc.*) and both C-C bond cleaved intermediate species (bicarbonate, formate, *etc.*) (steps in (2) and (3)), which were detected over Pd<sub>9</sub>Au<sub>9</sub> and Pd<sub>55</sub>Au<sub>45</sub>/Al<sub>2</sub>O<sub>3</sub> with the relative abundances depending on the bimetallic composition. Further decomposition of oxy-carbon species in an oxidative environment leads to their release, forming CO<sub>2</sub> and H<sub>2</sub>O (steps in (4)).

To aid the understanding of the surface interactions and reactivities, DFT calculations using a small AuPd cluster model with 13 atoms were performed to assess the relative stability of the clusters and the adsorption energy of propane,  $O_2$ , and some intermediate species. Fig. 8 show the calculated adsorption energy for molecularly-adsorbed oxygen and propane, and intermediate acetate species on  $Pd_{13-n}Au_n$  clusters. Details are summarized in Table S3, ESI,† along with additional calculation results for  $CH_3COO$ ,  $CH_3CH_2CH_2$ , and  $CH_3CHCH_3$  species on the cluster surfaces. The binding energy of the  $Au_nPd_{13-n}$  cluster follows the order  $Au_{13} < Pd_4Au_9 < Pd_7Au_6 < Pd_{12}Au_1 = Pd_{13}$ , showing a decrease in binding energy as Au% increases (Table S4, ESI†).

As shown in Fig. 8A, the adsorption energy for propane on the AuPd cluster model is very small, indicating very weak physical adsorption of propane on these clusters. In correlation with the experimentally observed maximum activity for the catalyst with Pd: Au ~50, the adsorption energy for propane over Pd<sub>4</sub>Au<sub>9</sub> and Pd<sub>7</sub>Au<sub>6</sub> is at a maximum. Similarly, the molecular adsorption of O2 was evaluated based on the Yeager model (Fig. 8B), revealing an intermediate adsorption energy for O2 on Pd7Au6. The weak interaction between O2 and the Au<sub>13</sub> cluster was previously reported to result in a very low adsorption energy.65 Interestingly, Fig. 8C reveals a minimum adsorption energy of acetate species on the Pd<sub>7</sub>Au<sub>6</sub> cluster. In comparison with the weak but maximized adsorption energy for propane over Pd7Au6, there is a strong but minimized adsorption energy for intermediate acetate species over Pd7Au6. The calculated adsorption energy for acetate over Pd7Au6 is indeed very small, which suggests weak adsorption of this species on the catalyst. However, the observed high DRIFTs intensity of acetate could suggest that acetate was relatively stable and underwent slow conversion into CO2. This correlation in combination with the intermediate adsorption energy for O2 over Pd7Au6 is thus believed to be responsible for the experimentally observed catalytic synergy in terms of the bimetallic composition. Note that the adsorption site features a 2-fold Pd site for Pd<sub>13</sub>, Pd<sub>12</sub>Au<sub>1</sub>, and Pd<sub>7</sub>Au<sub>6</sub> clusters, and a 2-fold Pd-Au site for the Pd<sub>4</sub>Au<sub>9</sub> cluster, suggesting the importance of the Pd-Pd surface adsorption site near Au atoms for the catalytic synergy. It is important to note that the DFT result was based on a 13-atom cluster model due to the limitation of our DFT calculation which, however, provides substantial information on the adsorption site and adsorption energy.

## 4. Conclusion

In conclusion, we have demonstrated for the first time that alloying Pd with Au in a catalyst with an optimal composition can enhance its catalytic activity for propane oxidation. The PdAu/TiO $_2$  catalysts were shown to exhibit not only an enhanced catalytic oxidation activity but also a strong composition dependence of the catalytic activity. The results have revealed not only an activity maximum at an  $\sim 50:50$  Pd:Au ratio in terms of reaction temperature but also a composition-dependent sensitivity to the thermochemical

treatment depending on the Au% in the NPs. The relative amounts of the none or 1st C-C bond cleaved oxidation species (acetone, ester, and acetate) to complete (1st and 2nd) C-C bond cleaved oxidation species (formate, bicarbonate) depend strongly on the bimetallic composition. The activity maximum at an ~50:50 Pd:Au ratio is believed to be linked to the weak but maximum adsorption energy for propane and strong but minimum adsorption energy for intermediate species, as well as the intermediate adsorption energy for O<sub>2</sub>. While the activity for nanoalloys with  $n \sim 50$  showed little change after the thermochemical treatment under oxygen, the activities for nanoalloys with n < 50 and n > 50 showed opposite trends. In comparison with Pd-rich PdAu alloys on Al<sub>2</sub>O<sub>3</sub>, the absence of adsorbed formate species and the reduced amount of adsorbed bicarbonate species over PdAu/  $Al_2O_3$  with  $\sim 50:50$  Pd: Au ratio are linked to the higher activity in terms of achieving a complete C-C cleavage of propane towards CO2 release. The combination of the lower surface oxophilicity in retaining the adsorbed intermediate formate and bicarbonate species and the increased lattice shrinking is believed to play an important role in the enhanced catalytic activity. It is also believed that the strong nanoalloy-support interaction for low- and medium-Au containing PdAu/TiO2 constitutes the basis for the catalytic synergy, which, upon further probing of the surface sites, will provide new insights into the design of nanoalloy catalysts for low-temperature hydrocarbon oxidation.

### Conflicts of interest

There are no conflicts to declare.

# Acknowledgements

This work was supported by the DOE-BES Grant (DESC0006877) and the National Science Foundation Fund (CHE 1566283). It was also in part supported by the Department of Education - Graduate Assistance in Areas of National Need. Work at the Advanced Photon Source was supported by DOE under Contract DE-AC02-06CH11357. Thanks are also due to 1-ID beamline staff for their help with the HE-XRD experiment.

### References

- 1 M. Baldi, E. Finocchio and F. Milella, *Appl. Catal., B*, 1998, 16, 43–51.
- 2 C.-H. Lai, C.-C. Chang, C.-H. Wang, M. Shao, Y. Zhang and J.-L. Wang, *Atmos. Environ.*, 2009, 43, 1456–1463.
- 3 J. J. Spivey, Ind. Eng. Chem. Res., 1987, 26, 2165-2180.
- 4 S. C. Kim and W. G. Shim, Appl. Catal., B, 2009, 92, 429-436.
- 5 D. Papageorgopoulos, M. Keijzer, J. Veldhuis and F. De Bruijn, *J. Electrochem. Soc.*, 2002, 149, 1400–1404.
- 6 W. S. Epling and G. B. Hoflund, J. Catal., 1999, 182, 5-12.
- 7 D. M. Fernandes, C. F. Scofield, A. A. Neto, M. J. B. Cardoso and F. M. Z. Zotin, *Process Saf. Environ. Prot.*, 2009, 87, 315–322.

- 8 R. Fang, Y. Cui, Z. Shi, M. Gong and Y. Chen, *Chin. J. Catal.*, 2015, 36, 994–1000.
- 9 C.-W. Yi, K. Luo, T. Wei and D. Goodman, J. Phys. Chem. B, 2005, 109, 18535–18540.
- 10 X. Y. Lang, H. Guo, L. Y. Chen, A. Kudo, J. S. Yu, W. Zhang, A. Inoue and M. W. Chen, J. Phys. Chem. C, 2010, 114, 2600–2603.
- 11 S. Xie, J. Deng, S. Zang, H. Yang, G. Guo, H. Arandiyan and H. Dai, J. Catal., 2015, 322, 38–48.
- 12 P. Yu, M. Pemberton and P. Plasse, *J. Power Sources*, 2005, 144, 11–20.
- 13 C. Descorme, R. Taha, N. Mouaddib-Moral and D. Duprez, *Appl. Catal.*, A, 2002, 223, 287–299.
- 14 K. Okumura, T. Kobayashi, H. Tanaka and M. Niwa, Appl. Catal., B, 2003, 44, 325–331.
- 15 H. Yoshida, Y. Yazawa and T. Hattori, *Catal. Today*, 2003, 87, 19–28.
- 16 M. B. Griffin, A. A. Rodriguez, M. M. Montemore, J. R. Monnier, C. T. Williams and J. W. Medlin, J. Catal., 2013, 307, 111–120.
- 17 H. Kareem, S. Shan, F. Lin, J. Li, Z. Wu, B. Prasai, C. P. O'Brien, I. C. Lee, D. T. Tran and L. Yang, *Nanoscale*, 2018, 10, 3849–3862.
- 18 B. Wang, X. Wu, R. Ran, Z. Si and D. Weng, *J. Mol. Catal. A: Chem.*, 2012, 356, 100–105.
- 19 C. P. O'Brien and I. C. Lee, J. Catal., 2017, 347, 1-8.
- 20 W. L. Faria, C. A. Perez, D. V. César, L. C. Dieguez and M. Schmal, *Appl. Catal.*, *B*, 2009, 92, 217–224.
- 21 Ö. Metin, X. Sun and S. Sun, Nanoscale, 2013, 5, 910-912.
- 22 R. Loukrakpam, J. Luo, T. He, Y. Chen, Z. Xu, P. N. Njoki, B. N. Wanjala, B. Fang, D. Mott and J. Yin, *J. Phys. Chem. C*, 2011, 115, 1682–1694.
- 23 S. M. Oxford, P. L. Lee, P. J. Chupas, K. W. Chapman, M. C. Kung and H. H. Kung, *J. Phys. Chem. C*, 2010, 114, 17085–17091.
- 24 T. Egami and S. J. L. Billinge, *Underneath the Braggs' Peak*, Pergamon/Amsterdam, Netherlands, 2003.
- 25 S. Krishnamurthy, A. Esterle, N. C. Sharma and S. V. Sahi, Nanoscale Res. Lett., 2014, 9, 627.
- 26 V. Petkov, B. Prasai, S. Shastri, J.-W. Kim, S. Shan, H. R. Kareem, J. Luo and C. J. Zhong, *J. Phys. Chem. C*, 2017, 121, 7854–7866.
- 27 S. Sakthivel, M. Shankar, M. Palanichamy, B. Arabindoo, D. Bahnemann and V. Murugesan, Water Res., 2004, 38, 3001–3008.
- 28 S. Poulston, T. I. Hyde, H. Hamilton, O. Mathon, C. Prestipino, G. Sankar and A. W. Smith, *Phys. Chem. Chem. Phys.*, 2010, 12, 484-491.
- 29 K. Leeá Tan, J. Mater. Chem., 2001, 11, 2378-2381.
- 30 S. L. Hemmingson and C. T. Campbell, *ACS Nano*, 2017, 11, 1196–1203.
- 31 K. H. Hansen, T. Worren, S. Stempel, E. Lægsgaard, M. Bäumer, H.-J. Freund, F. Besenbacher and I. Stensgaard, *Phys. Rev. Lett.*, 1999, 83, 4120.
- 32 C. T. Campbell and Z. Mao, ACS Catal., 2017, 7, 8460–8466.

Paper

- 33 H. T. Li, L. F. Chen, X. Yuan, W. Q. Zhang, J. R. Smith and A. G. Evans, J. Am. Ceram. Soc., 2011, 94, 1551-2916.
- 34 H. Chen, P. Li, N. Umezawa, H. Abe, J. Ye, K. Shiraishi, A. Ohta and S. Miyazaki, J. Phys. Chem. C, 2016, 120, 5549-5556.
- 35 M. Ahmadi, F. Behafarid and B. R. Cuenva, Nanoscale, 2016, 8, 11635-11641.
- 36 S. Tosoni and G. Pacchioni, J. Phys. Chem. C, 2017, 121, 28328-28338.
- 37 S. Shan, V. Petkov, L. Yang, J. Luo, P. Joseph, D. Mayzel, B. Prasai, L. Wang, M. Engelhard and C. J. Zhong, J. Am. Chem. Soc., 2014, 136, 7140-7151.
- 38 M. N. Taylor, W. Zhou, T. Garcia, B. Solsona, A. F. Carley, C. J. Kiely and S. H. Taylor, J. Catal., 2012, 285, 103-114.
- 39 T. Maillet, C. Solleau, J. Barbier Jr and D. Duprez, Appl. Catal., B, 1997, 14, 85-95.
- 40 M. Li, D. Weng, X. Wu, J. Wan and B. Wang, Catal. Today, 2013, 201, 19-24.
- 41 Y. Li, X. Wang and C. Song, Catal. Today, 2016, 263, 22-34.
- 42 V. Petkov, Y. Maswadeh, A. Lu, S. Shan, H. Kareem, Y. Zhao, J. Luo, C. J. Zhong, K. Beyer and K. W. Chapman, ACS Appl. Mater. Interfaces, 2018, 10, 10870-10881.
- 43 B. D. Mukri, G. Dutta, U. V. Waghmare and M. Hegde, Chem. Mater., 2012, 24, 4491-4502.
- 44 Z. Ren, Z. Wu, W. Song, W. Xiao, Y. Guo, J. Ding, S. L. Suib and P.-X. Gao, Appl. Catal., B, 2016, 180, 150-160.
- 45 M. Skotak, Z. Karpiński, W. Juszczyk, J. Pielaszek, L. Kępiński, D. Kazachkin, V. Kovalchuk and J. d'Itri, J. Catal., 2004, 227, 11-25.
- 46 G. Saracco, F. Geobaldo and G. Baldi, Appl. Catal., B, 1999, 20, 277-288.
- 47 C.-W. Tang, L.-C. Hsu, S.-W. Yu, C.-B. Wang and S.-H. Chien, Vib. Spectrosc., 2013, 65, 110-115.
- 48 H. Deng, Y. Yu and H. He, J. Phys. Chem. C, 2015, 119, 3132-3142.
- 49 Z. D. Yigezu and K. Muthukumar, J. Anal. Appl. Pyrolysis, 2015, 114, 60-67.

- 50 J. van den Brand, O. Blajiev, P. Beentjes, H. Terryn and J. De Wit, Langmuir, 2004, 20, 6318-6326.
- 51 D. G. Rethwisch and J. Dumesic, Langmuir, 1986, 2, 73-79.
- 52 V. Ermini, E. Finocchio, S. Sechi and S. Rossini, Appl. Catal., A, 2000, 190, 157-167.
- 53 A. R. McInroy, D. T. Lundie, J. M. Winfield, C. C. Dudman, P. Jones and D. Lennon, Langmuir, 2005, 21, 11092-11098.
- 54 E. Finocchio, G. Busca, V. Lorenzelli and R. J. Willey, I. Chem. Soc., Faraday Trans., 1994, 90, 3347-3356.
- V. Petkov, S. Shan, P. Chupas, J. Yin, L. Yang, J. Luo and C. J. Zhong, Nanoscale, 2013, 5, 7379-7387.
- 56 S. Shan, V. Petkov, L. Yang, D. Mott, B. N. Wanjala, F. Cai, B. H. Chen, J. Luo and C. J. Zhong, ACS Catal., 2013, 3, 3075-3085.
- 57 E. Ozensoy, D. Herling and J. Szanyi, Catal. Today, 2008, 136, 46-54.
- 58 J. Wan, R. Ran, M. Li, X. Wu and D. Weng, J. Mol. Catal. A: Chem., 2014, 383, 194-202.
- 59 Y. Yu, H. He, X. Zhang and H. Deng, Catal. Sci. Technol., 2014, 4, 1239-1245.
- 60 E. K. Gibson, A. M. Beale, C. R. A. Catlow, A. Chutia, D. Gianolio, A. Gould, A. Kroner, K. M. Mohammed, M. Perdjon and S. M. Rogers, Chem. Mater., 2015, 27, 3714-3720
- 61 L. Delannoy, S. Giorgio, J. G. Mattei, C. R. Henry, N. El Kolli, C. Méthivier and C. Louis, ChemCatChem, 2013, 5, 2707-2716.
- 62 A. Hinz, M. Skoglundh, E. Fridell and A. Andersson, J. Catal., 2001, 201, 247-257.
- 63 M. Hasan, M. Zaki and L. Pasupulety, J. Phys. Chem. B, 2002, 106, 12747-12756.
- 64 H. Luo, X.-D. Wu, D. Weng, S. Liu and R. Ran, Rare Met., 2017, 36, 1-9.
- 65 F. Shojaei, M. Mousavi, F. Nazari and F. Illas, Phys. Chem. Chem. Phys., 2015, 17, 3659-3672.